Biomedical Physics &
Engineering Express

Endorsed by IPEM Institute of Physics and Engineering in Medicine
PURPOSE-LED PUBLISHING™

PAPER • **OPEN ACCESS**

Feasibility analysis of micro-structural ultrasound for scatterer reconstruction in medicine: an in silico study

To cite this article: Mirjam Colleen Rupinski *et al* 2026 *Biomed. Phys. Eng. Express* **12** 025008

View the article online for updates and enhancements.

You may also like

- Emerging innovations in polycaprolactone-chitosan-hydroxyapatite composite scaffolds for tissue engineering: a review
Mohammed Razzaq Mohammed
- LGDUnet: a dual-branch network for weakly supervised gland segmentation in H&E stained histopathological images
Shiqiang Han, Zuxuan Wang, Yanhong Ji et al.
- LMSA-net: a lightweight multi-scale attention network for eeg-based emotion recognition
Hao Yue, Hengrui Ruan and Yawu Zhao

This content was downloaded from IP address 213.197.173.186 on 08/10/2026 at 12:21

Biomedical Physics & Engineering Express

Check for updates

OPEN ACCESS

RECEIVED
23 July 2025

REVISED
23 January 2026

ACCEPTED FOR PUBLICATION
29 January 2026

PUBLISHED
12 February 2026

Original content from this work may be used under the terms of the Creative Commons Attribution 4.0 licence.

Any further distribution of this work must maintain attribution to the author(s) and the title of the work, journal citation and DOI.

PAPER

Feasibility analysis of micro-structural ultrasound for scatterer reconstruction in medicine: an in silico study

Mirjam Colleen Rupinski[1,3], **Hossein S Aghamiry**[2,3], **Stefan Klemmer Chandia**[2], **Tom Meyer**[2], **Dominik Geisel**[2] and **Heiko Tzschätzsch**[1,*]

[1] Institute of Medical Informatics, Charité—Universitätsmedizin Berlin, Corporate Member of Freie Universität Berlin and Humboldt-Universität zu Berlin, Berlin, Germany
[2] Department of Radiology, Charité—Universitätsmedizin Berlin, Corporate Member of Freie Universität Berlin and Humboldt-Universität zu Berlin, Berlin, Germany
[3] Shared first authorship.
[*] Author to whom any correspondence should be addressed.

E-mail: heiko.tzschaetzsch@charite.de

Keywords: ultrasound, image analysis, scatterer reconstruction, micrometer structure analysis, sparse regularization, ADMM

Abstract

Although quantitative ultrasound has crossed the threshold from research tool to routine clinical adjunct, current techniques still only interrogate tissue at the millimeter scale. Direct, micrometer-resolved insight into tissue structure, comparable to histology, remains an unmet need. The Scatterer Reconstruction (ScatRec) method, a non-stationary, deconvolution-based technique, shows promise in addressing this need. We improved the ScatRec algorithm and introduced three upgrades to improve its robustness: (i) Anisotropic total-variation, (ii) a Gaussian-noise fidelity term, and (iii) amplitude bound constraints. Additionally we bridge the gap to real work application by utilizing a spatially invariant point spread function. We then evaluated the enhanced reconstruction capabilities using *in silico* scatterer phantoms. For the first time, we analyzed the resolution limits with several two-scatterer phantoms with different scatterer distances. We tested the reconstruction quality and accuracy with phantoms containing randomly distributed scatterers and a signal-to-noise ratio (SNR) ranging from infinity to 10. Our two-scatterer phantoms showed that our proposed method at 18 MHz has an effective scatterer resolution of 38.5 μm × 156 μm in the axial and lateral directions, respectively, which is 2.6 times better than conventional B-mode. For randomly distributed scatterers, we quantified the reconstruction quality (measured by the normalized correlation coefficient, NCC) and the accuracy (indicated by the relative deviation of the effective acoustic concentration, EAC, compared to the ground truth). Compared to the original ScatRec, the NCC improved 3.7-fold, and the EAC 15.5-fold across realistic SNR of 40. Our feasibility analysis suggests that *in vivo* micro-structural ultrasound for scatterer reconstruction is within reach, opening a path toward "ultrasonic histology" for diseases that are currently diagnosed only by biopsy.

1. Introduction

Methods for comprehensive, quantitative, and non-invasive tissue characterization provide important information for medical diagnostics and therapy monitoring. These include, among others, techniques such as quantitative magnetic resonance imaging (e.g., T1-, T2-, and hepatic fat quantification), elastography and especially quantitative ultrasound (e.g., attenuation, speed of sound, backscatter-measurement and speckle statistics) [1].

Current real-world uses include the assessment of early-stage fatty liver disease, classification of thyroid tumors, lymph nodes, and monitoring early cancer response to neoadjuvant treatment, supporting more personalized medicine and potentially reducing the need for invasive biopsies. Major ultrasound manufacturers have integrated quantitative ultrasound packages for tissue characterization, expanding diagnostic capabilities in organs such as the liver, breast, and brain. Despite challenges in standardization and implementation, quantitative ultrasound is

© 2026 The Author(s). Published by IOP Publishing Ltd

increasingly complementing traditional imaging modalities in clinical practice [1–3].

Quantitative ultrasound provides valuable insights into tissue properties—mechanical, perfusion, and acoustic—but their spatial resolution is largely limited to the millimeter scale. Although some of these methods use models and assumptions to estimate microscopic parameters (e.g. scatterer size and effective scatter density) [4, 5] that represent the ensemble of the investigated pixel, a direct and non-invasive analysis at the microscopic scale is still not possible. However microscopic histological analysis of invasively obtained tissue samples is routinely used to obtain important diagnostic information for several medical diseases (e.g. metabolic dysfunction–associated steatohepatitis (MASH) and metabolic dysfunction–associated liver disease (MASLD)). The ultrasound resolution required for this cannot be achieved even with the latest image enhancements methods [6]. A non-invasive microstructural ultrasound analysis, offering histology-like insights, could add important value to the diagnosis of several medical diseases.

A promising method to achieve this is the Scatterer Reconstruction (ScatRec) method introduced by Mattausch and Goksel [7, 8]. ScatRec is an optimization method which was originally designed to reconstruct scatterer positions to subsequently generate simulated ultrasound images. These simulated ultrasound images were used for high-fidelity virtual training environments for sonographers with multiple viewing angles and transducer settings. Mattausch and Goksel demonstrated the effectiveness of ScatRec on a range of simulated ultrasound images, closely resembling real-world observations. Their studies also showed that the statistical properties of the scatterer maps, particularly their conformity with the Nakagami distribution (a powerful diagnostic parameter which describes the scatterer density diagnosis [9]), align well with expected real tissue characteristics.

We therefore hypothesize that the ScatRec method can be used to obtain scatterer maps for a micro-structural analysis of biological tissue, which provide histology-like insights for medical diagnosis. However, the resolution, quality, and accuracy of these scatterer maps have yet to be evaluated directly and on a microscopic scale.

To address this gap, we investigated in this study the potential of ScatRec for high-resolution tissue characterization: Using *in silico* scatterer phantoms, we (i) enhanced the original ScatRec optimization problem by incorporating more robust regularization, and physical bound constraints on scatterer amplitudes; (ii) comprehensively evaluated the resolution, quality, and accuracy of reconstructed scatterer maps; (iii) analyzed the noise (Gaussian distribution vs. salt-and-pepper) based on real data.

2. Method

2.1. Phantoms and RF data

Radio-frequency (RF) data were generated using the Field II program (version 3.30) [10, 11] using MATLAB (R2024, MathWorks, Natick, MA, USA). For all simulations, a linear transducer with the following parameters was set: 192 elements, 50 μm kerf, 156 μm pitch, 106 μm element width and 6.2 mm element height. Imaging parameters were: R1.2 18 MHz frequency, two-periods long, Hann-windowed ultrasound pulse, 40 MHz sampling frequency, 384 lines of sight, 10 mm focus depth, 7 beam-steering angles from $-22°$ to $22°$ and Hamming apodization (FWHM 101 elements). Tissue was modeled with a constant speed of sound of 1540 m s^{-1} and no attenuation, because the spatial effects can be assumed to be approximately constant within the RF data region used for ScatRec (1×1 mm^2). The nominal axial and lateral resolutions of the post-beamformed RF data were 19.25 μm and 78.00 μm, respectively.

For resolution analysis, two series of five phantoms were created, each containing two scatterers with intensity 1 placed at 11 mm depth. One series varied the axial distances between scatterer centers from 38.5 μm (one pixel spacing) to 193 μm, while the other varied the lateral distances similar from 156 μm to 780 μm. To demonstrate the maximum achievable performance of ScatRec, no noise was added to the RF data generated from these phantoms.

For quality and accuracy analyses, 50 phantoms with scatterer densities of 5, 10, 20, 40, and 80 scatterers per mm^2 were generated. Scatterers were randomly uniform distributed within a 1×1 mm^2 region centered at 11 mm depth. The scatterer intensities were uniformly distributed between 0 and 1. Gaussian distributed noise with signal-to-noise ratios (SNR) of infinity, 80, 40, 20, and 10 was added to the RF data from these phantoms. The SNR was defined as the ratio of the maximum envelope amplitude of the RF data (without logarithmic compression) to the standard deviation of the noise.

2.2. ScatRec: Background

In ultrasound imaging, speckle formation arises from the coherent summation of scattered echoes within a resolution cell, often modeled by convolving an unknown distribution of sub-wavelength scatterers with point-spread functions (PSFs) [12, 13] which generally depends on the scatterer location. This model underlies ScatRec, which aims to estimate the tissue scatterer distribution directly from measured ultrasound RF data.

Concretely, we treat the ultrasound speckle pattern as a linear system of unknown "point" amplitudes subject to a known or estimated PSF. We have the mapping

$$\mathrm{A}\,\mathrm{x} = \mathrm{b}, \tag{1}$$

where $\mathbf{x} \in \mathbb{R}^n$ denotes the unknown scatterer amplitudes for each position, $\mathbf{b} \in \mathbb{R}^m$ represents the

measured RF data, and $\mathbf{A} \in \mathbb{R}^{m \times n}$ has the vectorized PSFs in its columns. Accurate estimation of the PSF can be achieved via calibration experiments or cepstrum-based approaches as described in detail by [14]. In real-world scenarios, the PSF can only be calculated for scatterers within a certain area (about mm^2 to cm^2), rather than for each scatterer individually (μm-resolved position). Therefore, we use the same PSF shape for all scatterer positions.

Given an ultrasound RF image $\mathbf{b}$ (or multiple such images) and the forward operator $\mathbf{A}$, the inverse problem is to recover $\mathbf{x}$ by solving $\mathbf{A}\,\mathbf{x} = \mathbf{b}$. Basically, such a model is ill-posed, and naive solutions can lead to unphysical or oscillatory results. To mitigate ill-posedness, ScatRec employs multiple observations of the same underlying scatterer distribution by changing certain imaging parameters. For example, beam steering collects several RF images $\mathbf{b}_i$ of the same tissue region from slightly different angles (-22° to $+22^\circ$), each satisfying

$$\mathbf{A_i}\,\mathbf{x} = \mathbf{b_i}, \tag{2}$$

where A_i corresponds to the forward operator (or PSF) for the i-th angle. Concatenating these systems yields:

$$\begin{bmatrix} \mathrm{A}_1 \\ \mathrm{A}_2 \\ \vdots \\ \mathrm{A}_N \end{bmatrix} \mathrm{x} = \begin{bmatrix} \mathrm{b}_1 \\ \mathrm{b}_2 \\ \vdots \\ \mathrm{b}_N \end{bmatrix} \Rightarrow \tilde{\mathrm{A}}\,\mathrm{x} = \tilde{\mathrm{b}}, \tag{3}$$

with $\tilde{\mathbf{A}}$ and $\tilde{\mathbf{b}}$ stacking the $\mathbf{A}_i$ and $\mathbf{b}_i$, respectively and N as the number of steering angles. Such multi-angle acquisitions reduce ambiguity and improve solution stability.

To further constrain the problem, ScatRec imposes sparsity prior and non-negativity as by Mattausch and Goksel [8]:

$$\min_{\mathbf{x} \geqslant 0} \; \|\tilde{\mathbf{A}}\,\mathbf{x} - \tilde{\mathbf{b}}\|_1 + \lambda \, \|\mathbf{x}\|_1, \tag{4}$$

where the data fidelity term $\|\tilde{\mathbf{A}}\,\mathbf{x} - \tilde{\mathbf{b}}\|_1$ confers robustness to outliers and is suitable for salt-and-pepper noise. Also, the ℓ_1-norm regularization on $\mathbf{x}$ and non-negativity promotes sparsity in the reconstructed model. It is also worth noting that YALL1, a solver based on the alternating direction method of multipliers (ADMM) [15], was originally utilized for this ℓ_1-regularized problem [16]. This approach has shown promising results for producing physically plausible scatterer maps from both *in vivo* and phantom data [14].

2.3. Enhanced ScatRec

Building on ScatRec, we propose three advancements: (1) Anisotropic total-variation (TV) regularization [17] (2) ℓ_2-norm for the fidelity term and (3) Bound constraints leveraging physical priors.

1. **Anisotropic TV Regularization:** Instead of a pure ℓ_1 (Lasso) penalty, we employ an anisotropic TV regularization, which promotes piecewise constant solutions while preserving sharp edges and boundaries [17]. The anisotropic TV regularizer is defined as: $\lambda \, \|\nabla_a \mathbf{x}\|_1 + \lambda \, \|\nabla_l \mathbf{x}\|_1$,

   where ∇_a and ∇_l represents the spatial gradient of the scatterer map in axial (a) and lateral (l) directions, respectively. This choice is motivated by the physical nature of scatterers in biological tissue: unlike idealized point, real scatterers have spatial extent and typically occupy multiple pixels in the reconstructed map. Standard ℓ_1 (Lasso) regularization promotes pixel-wise sparsity, treating each pixel independently, which can lead to fragmented or overly sparse representations that do not reflect the true spatial structure of scatterers. In contrast, TV regularization encourages spatial coherence by penalizing variations between neighbouring pixels, thereby promoting compact, connected regions with sharp boundaries which is a more realistic model for biological scatterers (e.g. fat vacuoles, or collagen fiber bundles). Unlike the ℓ_2 regularization family which over-smooths edges, anisotropic TV maintains sharp transitions between regions while suppressing noise within homogeneous areas. The directional gradients allow for different regularization strengths in axial versus lateral directions, accommodating the anisotropic nature of ultrasound PSFs and the potentially different resolution characteristics in these directions.

2. **ℓ_2-norm for the fidelity**: We assume a random noise with a Gaussian distribution and hence an ℓ_2-based data fidelity rather than the original ℓ_1 norm in ScatRec [14]. The reason for this selection will be described in the results section under "*Reference SNR estimation*".

3. **Bound Constraints:** Finally, we incorporate bound constraints $\mathbf{l} \leqslant \mathbf{x} \leqslant \mathbf{u}$. These constraints reflect known physical limits or valid amplitude ranges, complementing the earlier nonnegativity requirement.

Combining these modifications yields the following optimization problem:

$$\min_{\mathbf{x}} \; \lambda \, \|\nabla_a \mathbf{x}\|_1 + \lambda \, \|\nabla_l \mathbf{x}\|_1 \text{ subject to } \begin{cases} \mathbf{A}\,\mathbf{x} = \mathbf{b} \\ \mathbf{l} \leqslant \mathbf{x} \leqslant \mathbf{u} \end{cases}. \tag{5}$$

Here, $\lambda \geqslant 0$ controls the anisotropic TV regularization strength. For simplicity in notation, we drop the tildes and write $\mathbf{A}$ and $\mathbf{b}$, instead of $\tilde{\mathbf{A}}$ and $\tilde{\mathbf{b}}$.

To solve the enhanced ScatRec optimization problem efficiently, we employed the ADMM [15] approach. This method allows effective handling of large-scale and constrained optimization problems, facilitating the incorporation of non-smooth regularizations like TV, and also the box constraints. A

detailed mathematical formulation and implementation steps are provided in Appendices I and II.

In summary, these enhancements (anisotropic TV regularization, ℓ_2 fidelity and bound constraints) yield a robust extension of ScatRec that consistently recovers stable scatterer distributions under different imaging conditions. Proper parameter tuning yields to $\lambda = 0.01$, $\mathbf{l} = 0$ and, $\mathbf{u} = \text{inf}$ and further refines reconstruction quality across various signal-to-noise ratios and scatterer densities.

R2.2 Both our implementation of the original algorithm from Mattausch and Goksel. and our proposed algorithm are available on GitLab https://gitlab.com/Charite-IMI/scatrec.

2.4. Resolution metrics

The axial and lateral resolutions in B-mode were defined as the smallest distance between two scatterers that enabled distinct separation in the RF envelope, characterized by a local minimum within the gap lower than 50% of the peak amplitude. The axial and lateral resolutions in the reconstructed scatterer map were defined as the minimum distances at which two scatterers could be clearly distinguished.

2.5. Scatterer map quality and accuracy metrics

The quality of the reconstructed scatterer map $\mathbf{X} \in \mathbb{R}_+^{a\times l}$ compared to the ground-truth scatterer map $\mathbf{X}_{\text{GT}} \in \mathbb{R}_+^{a\times l}$ was calculated using the normalized correlation coefficient (NCC). The ground-truth scatterer map was calculated by distributing the intensity of each scatterer to the four surrounding pixels around its true (off-grid) scatter position. The four corresponding weightings w_i were calculated using the linear distance to the pixel positions with $\sum_{i=1}^{4} w_i = 1$. Please note here $\mathbf{X}$ is the 2D version of the optimization variable $\mathbf{x}$ which is originally a vector. An NCC value of 0 indicates very low reconstruction quality, whereas a value of 1 indicates excellent quality. Also $\overline{\mathbf{X}}$ is the mean value over all pixels in axial and lateral directions.

$$NCC = \frac{\sum_{a,l} |\mathbf{X} - \overline{\mathbf{X}}|\,|X_{\text{GT}} - \overline{\mathbf{X}_{\text{GT}}}|}{\sqrt{\sum_{a,l} |\mathbf{X} - \overline{\mathbf{X}}|^2 \cdot \sum_{a,l} |\mathbf{X}_{\text{GT}} - \overline{\mathbf{X}_{\text{GT}}}|^2}} \tag{6}$$

$$\overline{\mathbf{X}} = \frac{\sum_{a,l} \mathbf{X}}{\sum_{a,l} 1}$$

The accuracy of the reconstruction was calculated using the effective acoustic concentration (EAC) as

$$EAC = \frac{\sum_{a,l} \mathbf{X}}{d_a\, d_l \sum_{a,l} 1}. \tag{7}$$

Where $d_a = 19.25$ μm and $d_l = 78.00$ μm are the pixel sizes in the axial and lateral direction, respectively and thus the denominator is normalized by the corresponding area. Finally, the accuracy was estimated by the relative deviation from EAC to EAC_{GT}.

2.6. Nakagami m estimation

The Nakagami m parameter, which describes the scatterer density within a certain region of interest, can be calculated directly from the envelope of the RF data as [18]:

$$m = \frac{[\text{E}_{\text{Space}}(\boldsymbol{B}^2)]^2}{\text{E}_{\text{Space}}([\boldsymbol{B}^2 - \text{E}_{\text{Space}}(\boldsymbol{B}^2)]^2)} \tag{8}$$

$$m = \frac{[\text{E}_{\text{Space}}(\boldsymbol{B}^2)]^2}{\text{Var}_{\text{Space}}(\boldsymbol{B}^2)}$$

where $\mathbf{B}$ is the envelope of RF data (the 2D version of $\mathbf{b}$), E is the expectation operator and Var the variance operator. For each phantom, the m parameter was estimated over a 1×1 mm^2 area. However, the ground-truth m parameter m_0 was obtained over a larger area of 3×12 mm^2, which provided a large sample size of pixels to reach limit statistics, while still exhibiting homogeneous brightness. Since we simulate only random scatterers, the Nakagami m parameter should be tend to 0 for few scatterers and to 1 for many scatterers. Note that for pure Gaussian noise the Nakagami m should be 1.

2.7. Reference SNR estimation

To characterize the noise typically encountered in real ultrasound measurements, we conducted a noise test. We used an real world setting similar to our *in silico* simulation (device: Telemed ArtUs EXT-1H, Vilnius, Lithuania; transducer parameters: linear transducer L18-7H30-A5, 192 elements, pitch 156 μm, element height 6.2 mm; imaging parameters: center frequency 18 MHz, sampling frequency 40 MHz, number of lines of sight 384, focus 10 mm, power 0 dB) and investigated a CIRS phantom (Elasticity QA phantom model 049; CIRS, Norfolk, VA). These ultrasound imaging properties cover the typical values used in clinical settings to investigate superficial soft tissue, such as, breasts, lymph nodes, and thyroid. The transducer was mounted on a stand to avoid movement. 500 frames were acquired, and the RF envelope $\mathbf{B}$ was calculated using the axial Hilbert transform. The SNR map was estimated by pixel-wise division of the temporal mean of the envelope by the temporal standard deviation of the RF data. SNR values were averaged within a manually drawn region of interest centered at 11 mm depth.

$$SNR = \frac{\text{E}_{\text{Time}}(\mathbf{B})}{\sqrt{\text{Var}_{\text{Time}}(\mathbf{RF})}} \tag{9}$$

2.8. Performance analysis

To test the performance of ScatRec in terms of quality and computation time, we used one *in silico* phantom with 20 scatterers per mm^2 and a SNR of 20. For the

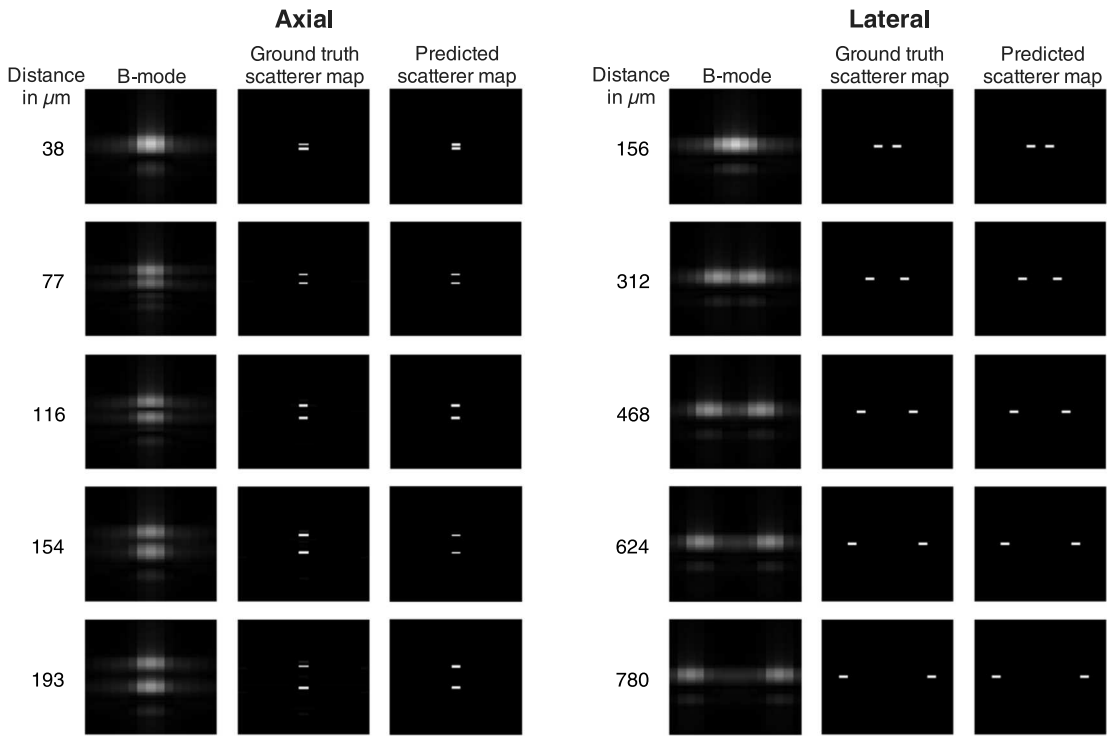


Figure 1. Resolution test for different scatterer distances with corresponding B-mode (all equally scaled), ground truth scatterer map and reconstructed scatterer map (all scaled from 0 to 1). In the B-mode, a separation was given when the scatterer distance was $\geqslant$ 102 μm and $\geqslant$ 402 μm for axial and lateral directions, respectively. In the reconstructed scatterer map, a separation was given for a distance equal to twice the nominal resolution of 19.25 μm × 78.00 μm in axial and lateral direction, respectively. Please note the interferences in B-mode which cause intensity alteration.

reconstruction, we used four combinations: two nominal reconstruction resolutions of 19.25 μm × 78.00 μm and 77.00 μm × 78.00 μm combined with N = 1 (ScatRec1, 0°) and N = 7 (ScatRec7, −22° to 22°) beam steering angles. We compared the resulting NCC, EAC and reconstruction time (system characteristics: AMD EPYC™ Milan, 3 GHz, 64 cores RAM 21 GB).

3. Results

3.1. Resolution test

In B-mode (envelope of the RF data without logarithmic compression), the FWHM of the single scatterer was 120 μm and 249 μm in the axial and lateral directions, respectively (see figure 1). Furthermore, visual separation was possible at distances greater than 102 μm and 402 μm in the axial and lateral directions, respectively. The achieved effective scatterer map's resolution in the axial and lateral directions was 38.5 μm × 156 μm, which corresponds to one pixel between the scatterers..

3.2. Quality and accuracy test

The quality and accuracy of the scatterer reconstruction was highest for noise-free data and decreased with increasing noise (see figures 2 and 3). With increasing scatterer density, the quality (NCC) of the reconstruction decreased slightly, but the accuracy (EAC) increased (smaller deviation from perfect accuracy).

In order to quantify the improvement in comparison with the previous method of Mattausch and Goksel and to Nakagami, we have calculated the error (absolute deviation from the perfect value) for the SNR values of 40, which cover the *in vivo* range and for worse SNR of 20 (see table 1).

3.3. Reference SNR estimation

B-mode image and the spatial distribution of the SNR across the imaging region is presented in figure 4. By analyzing data within the focal region (red rectangle, figure 4) and computing the histogram, we derived the noise distribution, which closely matches a Gaussian distribution. These results confirm that random noise with a Gaussian distribution provides a better approximation of the actual noise compared to the long-tail distribution assumed in the original ScatRec method [14] and consequently ℓ_2-norm for the fidelity term. An SNR value of 38 (31 dB, respectively) was obtained at a center frequency of 18 MHz.

3.4. Performance test

The results of the performance test are shown in figure 5 and table 2. Overall, ScatRec7 showed higher NCC and EAC/EAC$_0$ values as well as higher processing time compared to ScatRec1. Additionally, the nominal reconstruction resolution of 19.25 μm × 78.00 μm showed higher NCC, EAC/EAC$_0$ values with higher deviation from the perfect

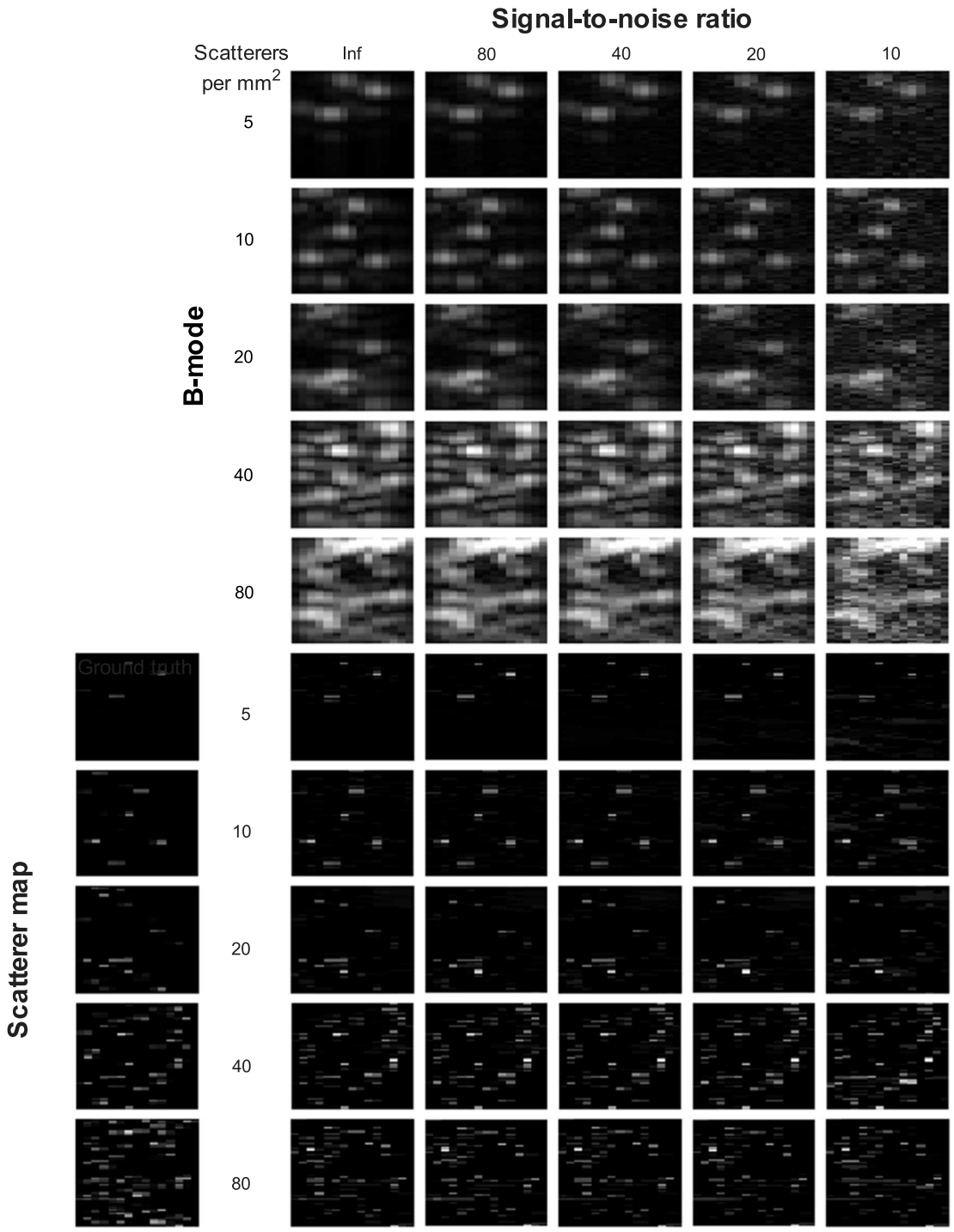


Figure 2. Comparison of B-mode and corresponding scatterer reconstruction with the ground truth for different scatterer densities and signal-to-noise ratios. All scatterer maps have the same scale of 0 to 1 and a side length of 1 μm.

accuracy, as well as higher processing time compared to 77.00 μm × 78.00 μm.

4. Discussion

In this study, we introduced and validated for the first time micro-structural ultrasound for the analysis of scatterers on a microscopic scale. Our work is based on the developments of Mattausch and Goksel [7, 8], but goes beyond their scope by analyzing the scatterer reconstruction itself rather than the resulting B-mode and significantly improving the reconstructed scatterer quality and accuracy by our proposed reconstruction algorithm. In particular, we have shown that the theoretical effective scatterer resolution for the given parameters is 38.5 μm × 156 μm (2 times the nominal resolution), about 2.6 times better than in B-mode. Even for scenarios with realistic noise and more than two scatterers, the proposed method yielded good and sufficient reconstruction quality (NCC of 0.70-0.91). Only for very high Noise ($\leqslant$ 10)

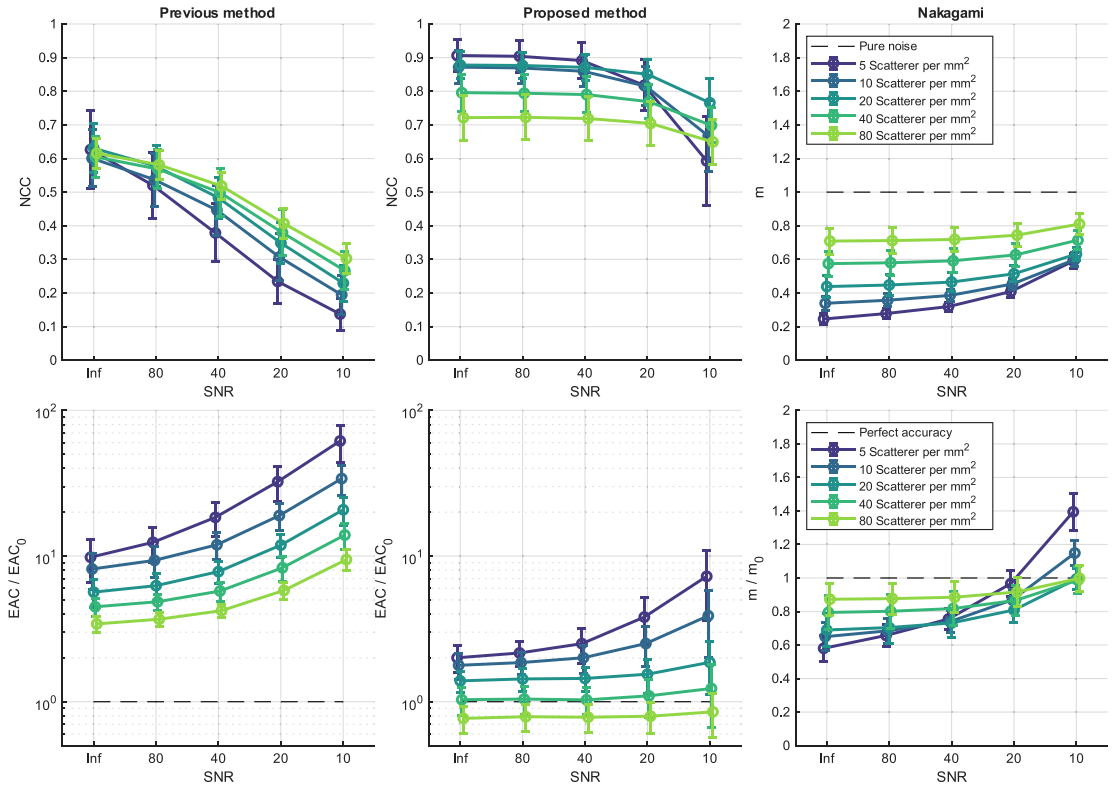


Figure 3. Scatterer reconstruction quality (NCC) and accuracy (EAC/EAC_0) for different signal-to-noise ratios (SNR) and different scatterer densities. In Comparison, the Nakagami m and the corresponding accuracy (m/m_0) is shown. Values as shown in mean and standard deviation of 50 independent simulations. EAC_0 and m_0 are calculated by the mean based on the noise free data.

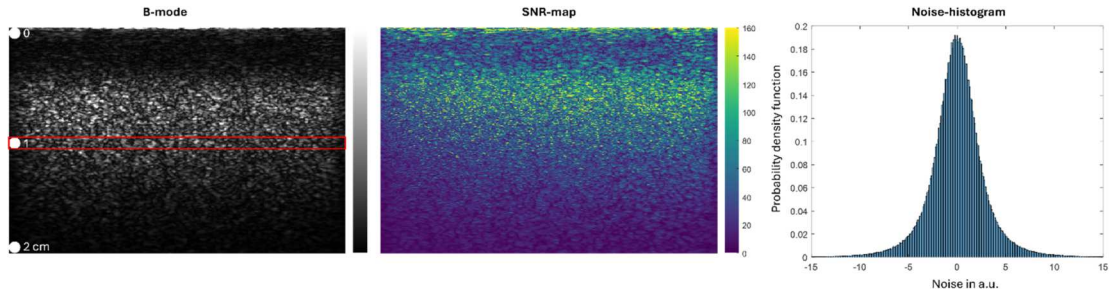


Figure 4. Representative B-mode ultrasound image of the homogeneous phantom with corresponding spatial distribution of SNR and histogram showing the noise distribution within the region of interest around the focus (red rectangle). Noise values were computed by subtracting the temporal mean from each RF-data pixel before analysis.

Table 1. Error (absolute deviation from the perfect value) for the method of Mattausch *et al*, the proposed method and for Nakagami. NCC represents the quality, EAC/EAC_0 the accuracy and m the Nakagami parameter. EAC_0 and m_0 are calculated by the mean based on the noise free data.

		Median [min, max]	
Metric	Method	SNR = 40	SNR = 20
|1—NCC|	Previous	0.52 [0.48, 0.62]	0.65 [0.59, 0.77]
	Proposed	0.14 [0.11, 0.28]	0.19 [0.15, 0.30]
$\|1 - EAC/EAC_0\|$	Previous	6.82 [3.22, 17.43]	10.89 [4.81, 31.40]
	Proposed	0.44 [0.03, 1.50]	0.54 [0.10, 2.81]
$\|1 - m/m_0\|$	Nakagami	0.25 [0.11, 0.27]	0.13 [0.03, 0.19]

the quality was reduced. For random scattering, the Nakagami m is limited to 1 and a scatterer density of 80 per mm^2 already corresponds to a $m = 0.81$. All in all, it is still an open question as to how high the density of scatterers will be observed in real tissue. In general, the Nakagami m is a powerful parameter for

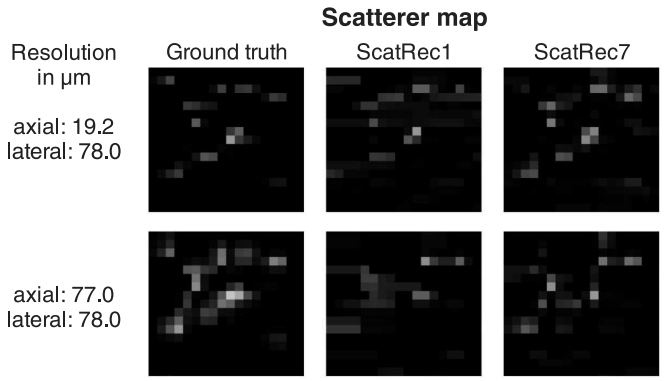


Figure 5. Comparison of the scatterer map quality for different reconstruction configurations of the same 1×1 mm^2 phantom with a signal to noise = 20 and a scatterer density of 20 mm^2. ScatRec1 and ScatRec7 are the reconstruction with N = 1 and 7 beam steering angles, respectively.

Table 2. Comparison of the reconstruction performance for different reconstruction configurations. NCC represents the quality and EAC/EAC$_0$ the accuracy. ScatRec1 and ScatRec7 are the reconstruction with N = 1 and 7 beam steering angles, respectively.

Resolution in µm	NCC		EAC/EAC$_0$		Processing time in s	
	ScatRec1	ScatRec7	ScatRec1	ScatRec7	ScatRec1	ScatRec7
19×78	0.73	0.88	1.56	1.67	6	78
77×78	0.51	0.66	0.51	0.66	1	4

diagnosis [9], its accuracy is compareable to the proposed method, but provides a resolution that is several times worse. Therefore, the diagnostic value of the proposed method lies in the interpretation of the geometric scatterer structure and the relative scatterer intensities rather than the calculation of macroscopic speckle characteristics, such as the scatterer density. For example, for the scoring of MASH and MASLD, the geometric localization of the fat vacuoles (near the central vein or near the portal vein and whether the distribution is homogeneous or heterogeneous) is a critical parameter [19]. Since the distance from central vein to the portal vein within the liver lobule is about 0.5–1.25 mm and the size of the hepatocytes is about 20–30 µm, a resolution similar to what we have achieved is necessary and sufficient. To achieve the same resolution with conventional B-mode, scanning acoustic microscopy or ultrasound localization microscopy, much higher ultrasound frequencies are required or only the perfusion could be analyzed, while the penetration depth decreases to a few millimeters [20, 21]. For clarity, our method is not an image enhancement method. It is designed to quantify and characterize the structure of the scatterer distribution. Therefore, the proposed method is to date the only method for microscopic analysis of clinical *in vivo* tissues in the future. This analysis (e.g., structural arrangement of scatterers and relative scatterer intensity) could provide important information for diagnosis [22]. Although our method might not achieve the resolution of a light microscope image of a biopsy sample, it has the potential to resolve microscopic tissue structures that could provide valuable information for medical diagnosis.

With regard to clinical applications, there are numerous: In oncology, these methods could enable early assessment of tumor response to chemotherapy by detecting microstructural changes before visible size reduction occurs, potentially allowing timely transition to second-line therapy [23]. The ability to characterize tissue microstructure has proven valuable in differentiating between benign and malignant breast tumors and monitoring treatment efficacy [2, 24]. Micro-ultrasound, which uses 29 MHz and provides B-mode with a resolution of about 70–100 µm, has also demonstrated equivalent performance to MRI for prostate cancer detection with improved visualization of tumor extent [25, 26]. In cardiovascular medicine, high-resolution reconstruction enables precise 3D visualization of coronary stents, supporting procedural optimization and advancement of stent technologies [27]. Real-time multiplanar reconstruction using 3D transesophageal echocardiography enhances precision during complex structural heart interventions [28]. For pulmonary applications, structural parameters from quantitative ultrasound show significant correlation with disease severity in fibrosis and edema, offering quantitative assessment tools for lung pathologies [29]. In tissue engineering, these techniques provide non-destructive, longitudinal monitoring of structural, biological, and mechanical properties of engineered constructs [30]. As stated, several medical

professions could potentially benefit from our proposed micro-structural ultrasound.

To improve robustness and generalization of our proposed method, we analyzed the noise distribution and adapted the ScatRec algorithm. Our analysis of the physical phantom confirmed that the real noise follows a Gaussian distribution. This insight was directly utilized to refine the reconstruction algorithm by replacing the ℓ_1-norm fidelity term with the ℓ_2-norm. Further improvements were introduced by incorporating anisotropic TV regularization, and bound constraints informed by physical priors. TV regularization enhances stability and robustness compared to Lasso (ℓ_1) regularization, particularly when dealing with spatially correlated features inherent in ultrasound imaging. While Lasso promotes pixel-wise sparsity and tends to create fragmented, isolated non-zero pixels scattered throughout the reconstruction, TV regularization exploits the spatial structure of the problem by penalizing variations between neighbouring pixels. This encourages spatially coherent, connected regions while preserving sharp boundaries. This is a critical advantage for reconstructing biological scatterers that have spatial extent (e.g. fat vacuoles, collagen fibers) rather than being idealized point sources. TV regularization leads to more physically plausible reconstructions with well-defined scatterer boundaries, and improved noise suppression within homogeneous regions. Unlike ℓ_2 family regularization, which over-smooths edges and blurs structural details, TV maintains sharp transitions between scatterers and background. Additionally, the anisotropic formulation allows for directional control, accommodating the different resolution characteristics in axial versus lateral directions inherent to ultrasound imaging, thereby producing reconstructions that better reflect the true microstructural geometry of tissue.

Finally, the bound constraints ensure that the estimated scatterer amplitudes remain within a predefined physical range. These adaptations improved both the quality and accuracy of the reconstruction by factors of 3.7 and 15.5, respectively, compared to the previous method (for SNR = 40). These enhancements were crucial in achieving a sufficiently resolved scatterer map within the expected *in vivo* SNR range.

The next step towards the *in vivo* application will be the validation using physical phantoms with known scatterer locations and increasing the reconstructed scatterer map area. For this purpose, our performance analysis provided reference information on the number of beam steering angles, the quality of the scatterer map and the processing time. A better resolution and higher number of steering angles will lead to better quality and resolution of the scatterer map but also to extended processing time. In our study, the processing time for the resolution of 19.25 μm $\times$ 78.00 μm and 7 beam steering angles is about 78 s, but the current reconstruction algorithm is not yet optimized for time. However, the required scatterer map resolution and quality must be specified based on the observed microscopic structure of the target diseases *in vivo*. Therefore, the next milestones to achieve the ultimate goal of establishing this method as a new diagnostic tool are: (i) estimating the PSF *in vivo* (e.g., using the method of Michailovich *et al* [6]); (ii) validating in physical phantoms; (iii) validating in *ex vivo* tissue samples (e.g., using light microscopy for ground truth); and (iv) demonstrating the diagnostic performance *in vivo* (e.g., via malign and benign lymph node tumors). Several challenges arise, particularly for *in vivo* applications: (i) The received amplitude of the RF data depends on individual attenuation and directly scales the reconstructed scatterer intensities (but not their position). To address this, the ultrasound attenuation could be corrected [31]; (ii) Individual tissue properties can affect the PSF, thereby reducing the reconstruction quality. To adapt PSF estimation locally, blind deconvolution could be used [6]. Additionally, blind deconvolution could reduce the noise effect on scatterer reconstruction; (iii) Tissue boundaries cause significant variation in PSF shape and intensity. Therefore, scatterer reconstruction should be restricted to locally homogeneous soft tissue; R2.1 (iv) Scatterer positions are not restricted to the image plane. However, the PSF of scatterers with increasing positions in the elevation direction is mainly characterized by reduced intensity rather than shape change. Therefore, the reconstructed scatterers are expected to be in the correct in-plane position, but with reduced intensity.

4.1. Limitation

A limitation of our study is that the effect of ultrasound frequency on resolution, quality and accuracy was not investigated. We hypothesize that the quality of the reconstructed scatterer map will improve with higher frequency. To find the trade-off frequency between sufficient penetration depth/SNR and scatterer map quality, future *in vivo* studies need to be performed. Another limitation of our study is our focus on *in silico* validation only. Therefore, the next steps will be to validate with physical phantoms and *in vivo* human tissue data.

5. Conclusion

The new microscopically resolved ultrasound method provides scatterer maps with an effective resolution of 38.5 μm $\times$ 156 μm and a very good reconstruction quality in the *in vivo* SNR range. Therefore, the proposed method is the first for non-invasive, microscopic and quantitative structural analysis of human tissues *in vivo*.

Acknowledgments

We thank the German Research Foundation (DFG) for funding (TM to CRC1340 Matrix in Vision, SK to

GRK2260 BIOQIC and TM to FOR5628 project number 513752256) and German Federation of Industrial Research Associations (AIF) for funding (HA to KK5611902 BM4). Open access funding enabled and organized by Projekt DEAL.

Data availability statement

The data cannot be made publicly available upon publication because they are not available in a format that is sufficiently accessible or reusable by other researchers. The data that support the findings of this study are available upon reasonable request from the authors https://gitlab.com/Charite-IMI/scatrec.

Appendix I. ADMM Formulation for the Enhanced ScatRec

We solve this composite objective via ADMM, a powerful technique for large-scale, constrained optimizations [15, 32]. To handle the ℓ_1 and the box constraints, we introduce an auxiliary variables $\mathbf{g_a} = \nabla_a \mathbf{x}$, $\mathbf{g}_l = \nabla_l \mathbf{x}$ (for TV regularization) and $\mathbf{z} = \mathbf{x}$ (for bound constraints). Then the problem becomes:

$$\min_{\mathbf{x},\ \mathbf{z},\ \mathbf{g_a},\mathbf{g}_l} \lambda \|\mathbf{g_a}\|_1 + \lambda \|\mathbf{g}_l\|_1$$

$$\text{subject to} \begin{cases} \mathbf{A}\,\mathbf{x} = \mathbf{b} \\ \mathbf{z} = \mathbf{x} \\ \mathbf{g_a} = \nabla_a \mathbf{x} \\ \mathbf{g}_l = \nabla_l \mathbf{x} \\ \mathbf{l} \leqslant \mathbf{z} \leqslant \mathbf{u} \end{cases}. \tag{A1}$$

Defining dual variables $\mathbf{u}$ (for $\mathbf{z} = \mathbf{x}$), $\boldsymbol{\nu}$ (for $\mathbf{A}\,\mathbf{x} = \mathbf{b}$), $\mathbf{d}_a$(for $\mathbf{g_a} = \nabla_a \mathbf{x}$), $\mathbf{d}_l$(for $\mathbf{g}_l = \nabla_l \mathbf{x}$) and letting ρ_1, ρ_2, $\rho_3 > 0$ be penalty parameters, the augmented Lagrangian is:

$$\begin{aligned} &\mathscr{L}_\rho(\mathbf{x}, \mathbf{z}, \mathbf{g_a}, \mathbf{g}_l, \mathbf{u}, \boldsymbol{\nu}, \mathbf{d}_1, \mathbf{d}_2) \\ =&\lambda \|\mathbf{g_a}\|_1 + \lambda \|\mathbf{g}_l\|_1 + \delta_{[\mathbf{l},\mathbf{u}]}(\mathbf{z}) \\ &+\tfrac{\rho_3}{2} \|\mathbf{g_a} - \nabla_a \mathbf{x} + \mathbf{d}_a\|_2^2 \\ &+\tfrac{\rho_3}{2} \|\mathbf{g}_l - \nabla_l \mathbf{x} + \mathbf{d}_l\|_2^2, \end{aligned} \tag{A2}$$

where $\delta_{[\mathbf{l},\mathbf{u}]}$ is the indicator function that is 0 if $\mathbf{l} \leqslant \mathbf{z} \leqslant \mathbf{u}$ component-wise and $+\infty$ otherwise. After tuning the parameter, the following parameters are used: $\lambda = 0.01$, $\rho_1 = 0.1$, $\rho_2 = \rho_3 = 0.03$, and we assume positivity bound constrains ($\mathbf{l} = 0$ and, $\mathbf{u} = \inf$).

In ADMM framework [15], primal and dual variables are updated in an alternating fashion. Specifically, at each iteration, a subset of the primal variables (in our case, $\mathbf{x}$, $\mathbf{z}$, $\mathbf{g_a}$ and $\mathbf{g}_l$) is treated as *active* and updated, while the remaining variables are held fixed. Once the primal variables are updated, the algorithm proceeds to update the dual variables ($\mathbf{u}$, $\boldsymbol{\nu}$, $\mathbf{d}_a$, and $\mathbf{d}_l$). This decoupled procedure often leads to robust convergence and handles large-scale or constrained problems more efficiently than classical single-step methods.

x-Update: Minimize the quadratic in $\mathbf{x}$:

$$\begin{aligned} &\min_{\mathbf{x}} \tfrac{\rho_1}{2} \|\mathbf{A}\,\mathbf{x} - \mathbf{b} + \boldsymbol{\nu}\|_2^2 + \tfrac{\rho_2}{2} \|\mathbf{z} - \mathbf{x} + \mathbf{u}\|_2^2 \\ &+ \tfrac{\rho_3}{2} \|\mathbf{g_a} - \nabla_a \mathbf{x} + \mathbf{d}_a\|_2^2 + \tfrac{\rho_3}{2} \|\mathbf{g}_l - \nabla_l \mathbf{x} + \mathbf{d}_l\|_2^2. \end{aligned} \tag{A3}$$

Taking the gradient and setting it to zero yields:

$$\begin{aligned} &(\rho_1\, \mathbf{A}^\top \mathbf{A} \ + \ \rho_2 \mathbf{I} + \rho_3\ \nabla_a^T \nabla_a + \rho_3\ \nabla_l^T \nabla_l) \\ &\mathbf{x} = \rho_1\, \mathbf{A}^\top (\mathbf{b} - \boldsymbol{\nu}) + \rho_2\, (\mathbf{z} + \mathbf{u}) \\ &+\rho_3\, \nabla_a^T (\mathbf{g_a} + \mathbf{d_a}) + \rho_3\, \nabla_l^T (\mathbf{g}_l + \mathbf{d}_l). \end{aligned} \tag{A4}$$

In large-scale problems, direct factorization of $\rho_1\, \mathbf{A}^\top \mathbf{A} \ + \ \rho_2 \mathbf{I} + \rho_3\ \nabla_a^T \nabla_a + \rho_3\ \nabla_l^T \nabla_l$ is expensive. Therefore, we solve this system using Krylov subspace methods, such as the Preconditioned Conjugate Gradient (PCG), where matrix-vector products are computed through function calls rather than explicit matrix formation.

z-Update (box-projection): Next, with $\mathbf{x}$, $\mathbf{u}$ fixed, A2 reduces to:

$$\min_{\mathbf{z}} \frac{\rho_2}{2} \|\mathbf{z} - \mathbf{x} + \mathbf{u}\|_2^2 + \delta_{[\mathbf{l},\mathbf{u}]}(\mathbf{z}), \tag{A5}$$

which is the projection of $\mathbf{x} - \mathbf{u}$ onto the interval $[\mathbf{l}, \mathbf{u}]$. The solution is the component-wise Euclidean projection (clipping) [32] as:

$$\Pi_{[l_i,u_i]}(z_i) = \min\{\, u_i,\ \max\{l_i,\ z_i\}\}. \tag{A6}$$

$\mathbf{g_a}$- and $\mathbf{g}_l$-update (TV in axial and lateral directions): With $\mathbf{x}$ and $\mathbf{d}_a$ fixed, A2 reduces to

$$\min_{\mathbf{g_a}} \lambda \|\mathbf{g_a}\|_1 + \frac{\rho_3}{2} \|\mathbf{g_a} - \nabla_a \mathbf{x} + \mathbf{d}_a\|_2^2, \tag{A7}$$

that is the proximal map of ℓ_1-norm. It decouples element-wise and admits a closed-form soft-thresholding:

$$g_a = \text{shrink}(\nabla_a \mathbf{x} - \mathbf{d}_a,\quad \lambda/\rho_3), \tag{A8}$$

where

$$\text{shrink}(\alpha,\ \beta) = \text{sign}(\alpha)\, \max(0,\ |\alpha| - \beta). \tag{A9}$$

Consequently, with fixed $\mathbf{x}$ and $\mathbf{d}_l$ the closed-form expression for g_l reads:

$$g_l = \text{shrink}(\nabla_l \mathbf{x} - \mathbf{d}_l,\quad \lambda/\rho_3). \tag{A10}$$

Dual Updates: Finally, we update the dual variables:

$$\begin{cases} \mathbf{u} \leftarrow \mathbf{u} + (\mathbf{z} - \mathbf{x}), \\ \boldsymbol{\nu} \leftarrow \boldsymbol{\nu} + (\mathbf{A}\,\mathbf{x} - \mathbf{b}), \\ \mathbf{d}_a \leftarrow \mathbf{d}_a + (\mathbf{g_a} - \nabla_a \mathbf{x}), \\ \mathbf{d}_l \leftarrow \mathbf{d}_l + (\mathbf{g}_l - \nabla_l \mathbf{x}), \end{cases} \tag{A11}$$

Convergence Criteria: We use two stopping conditions: (i) the *primal residual* $\|\mathbf{A}\,\mathbf{x}^{k+1} - \mathbf{b}\|_2$, where k indicate the iteration number, drops near an estimated noise level σ, which can be approximated by solving an unconstrained least-squares problem $\min_{\mathbf{x}} \|\mathbf{A}\,\mathbf{x} - \mathbf{b}\|_2$ via PCG and measuring the resulting residual norm , or (ii) the relative change in $\mathbf{x}$, $\mathbf{z}$,

Algorithm 1. ADMM for enhanced ScatRec.

Input: $\mathbf{A}$, $\mathbf{D}$, $\mathbf{b}$, $\mathbf{l}$, $\mathbf{u}$, λ, ρ_1, ρ_2, ρ_3, ε, maxIter
Initialize: $\mathbf{z}$, $\mathbf{g}_a$, $\mathbf{g}_l$, $\mathbf{u}$, $\boldsymbol{\nu}$, $\mathbf{d}_a$, $\mathbf{d}_l = 0$
For $k = 0,\ldots,$ maxIter:
- Solve the x-update using iterative Krylov methods (e.g., PCG).
- Update $\mathbf{g}_a$, $\mathbf{g}_l$ with soft thresholding.
- Update $\mathbf{z}$ with box projection.
- Update $\mathbf{u}$, $\boldsymbol{\nu}$, $\mathbf{d}_a$ and $\mathbf{d}_l$ (dual variables).
- Check stopping conditions: $\|\mathbf{A}\,\mathbf{x}^{k+1} - \mathbf{b}\|_2$ reaches near noise level or relative changes in $\mathbf{x}$, $\mathbf{z}$, $\mathbf{g}_a$, and $\mathbf{g}_l$ be less than ε.

$\mathbf{g}_a$, and $\mathbf{g}_l$ becomes sufficiently small (less than ε), indicating no further significant improvement.

Summarizing, we outline the ADMM procedure in Algorithm 1.

Appendix II. Subanalysis of the impact of two major changes on reconstruction quality

To investigate the individual contributions of our two major methodological changes: [1] anisotropic TV regularization and [2] ℓ_2-norm fidelity, we conducted an intermediate analysis comparing three approaches:

1. **Original method** (equation (4)): ℓ_1 regularization $+\,\ell_1$ fidelity [14].
2. **Intermediate method**: ℓ_1 regularization $+\,\ell_2$ fidelity.
3. **Proposed method** (equation (5)): Anisotropic TV regularization $+\,\ell_2$ fidelity.

Figure A1 presents representative reconstructions and quantitative metrics (NCC for quality and EAC/EAC$_0$ for accuracy) for these three approaches across different signal-to-noise ratios and scatterer densities. The first column shows results from the original method, the middle column displays the intermediate method with only the fidelity term modified, and the last column presents our proposed method. Additionally, figure A2 presents the corresponding scatterer maps for SNR of 40.

The results demonstrate that both modifications contribute complementary improvements to reconstruction quality. Specifically, replacing the ℓ_1 fidelity term with the ℓ_2 fidelity term (middle column) yields already improvements in both NCC and EAC metrics, which is consistent with our noise distribution analysis showing that ultrasound RF data follows a Gaussian distribution rather than exhibiting heavy-tailed,

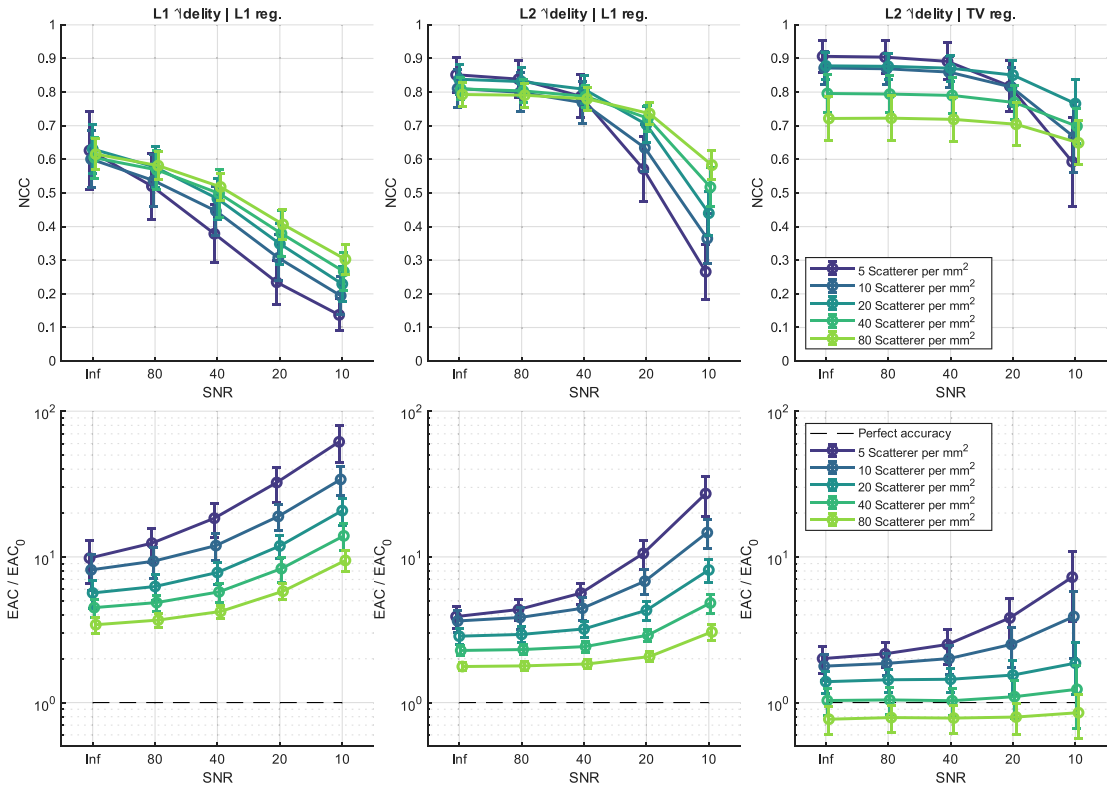


Figure A1. Effect of regularization type and fidelity norm on scatterer reconstruction quality. (Left) Original method using ℓ_1 regularization with ℓ_1 fidelity term. (Middle) Intermediate method using ℓ_1 regularization with ℓ_2 fidelity term. (Right) Proposed method using anisotropic TV regularization with ℓ_2 fidelity term. Rows show NCC (representing quality) and EAC/EAC$_0$ (representing accuracy) for different SNR and scatterer densities.

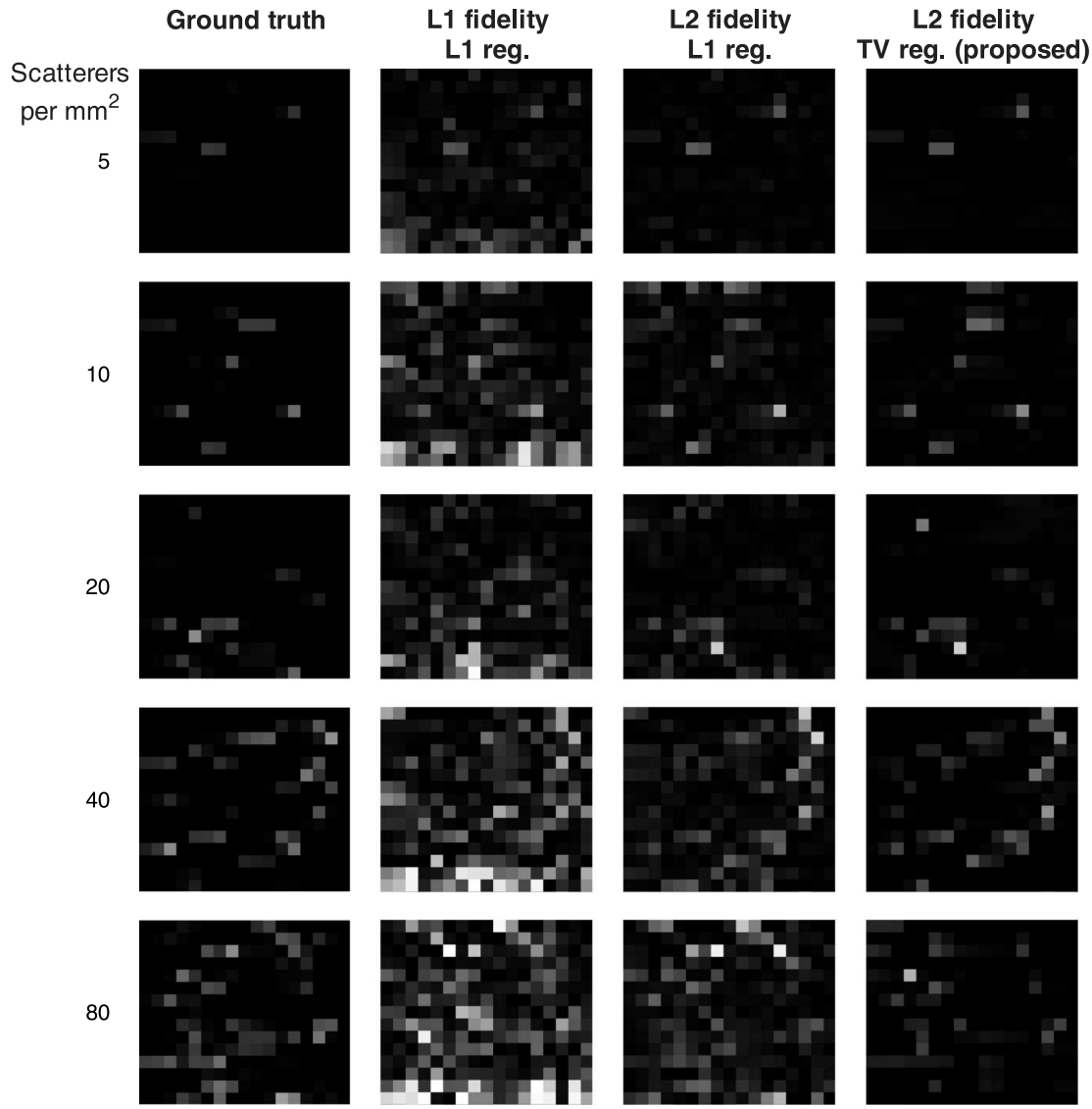


Figure A2. Effect of regularization type and fidelity norm on scatterer reconstruction map for SNR = 40 and scatterer densities. Ground truth scatterer map (1st column), Original method using ℓ_1 regularization with ℓ_1 fidelity term. (2nd column) Intermediate method using ℓ_1 regularization with ℓ_2 fidelity term. (3rd column) and proposed method using anisotropic TV regularization with ℓ_2 fidelity term (4th column).

salt-and-pepper noise. However, the most substantial improvement is achieved when additionally, substituting ℓ_1 regularization with anisotropic TV regularization (last column). This second modification promotes spatially coherent scatterer regions with preserved boundaries, leading to reconstructions that are both quantitatively more accurate and qualitatively more consistent with the expected spatial structure of biological tissue scatterers.

In summary, while the ℓ_2 fidelity term provides improved noise modeling, the anisotropic TV regularization delivers the primary enhancement in reconstruction quality by better capturing the spatial characteristics of tissue microstructure.

References

[1] Cloutier G, Destrempes F, Yu F and Tang A 2021 Quantitative ultrasound imaging of soft biological tissues: a primer for radiologists and medical physicists *Insights Imaging* **12** 127
[2] Khairalseed M and Hoyt K 2023 High-resolution ultrasound characterization of local scattering in cancer tissue *Ultrasound Med. Biol.* **49** 951–60
[3] Huang C *et al* 2021 Super-resolution ultrasound localization microscopy based on a high frame-rate clinical ultrasound scanner: an in-human feasibility study *Phys. Med. Biol.* **66** 15
[4] Zhou Z, Gao R, Wu S, Ding Q, Bin G and Tsui P-H 2024 Scatterer size estimation for ultrasound tissue characterization: A survey *Measurement* **225** 114046
[5] Oelze M L and Mamou J 2016 Review of quantitative ultrasound: envelope statistics and backscatter coefficient imaging and contributions to diagnostic ultrasound *IEEE Trans. Ultrason. Ferroelectr. Freq. Control* **63** 336–51

[6] Michailovich O V and Adam D 2005 A novel approach to the 2-D blind deconvolution problem in medical ultrasound *IEEE Trans. Med. Imaging* **24** 86–104
[7] Mattausch O and Goksel O 2016 Image-based PSF estimation for ultrasound training simulation *Simulation and Synthesis in Medical Imaging* (Springer) (https://doi.org/10.1007/978-3-319-46630-9_3)
[8] Mattausch O and Goksel O 2018 Image-based reconstruction of tissue scatterers using beam steering for ultrasound simulation *IEEE Trans. Med. Imaging* **37** 767–80
[9] Park J, Lee J M, Lee G, Jeon S K and Joo I 2022 Quantitative evaluation of hepatic steatosis using advanced imaging techniques: focusing on new quantitative ultrasound techniques *Korean J Radiol.* **23** 13–29
[10] Jensen J A 1997 Field: a program for simulating ultrasound systems *Med. Biol. Eng. Comput.* **34** 351–3
[11] Jensen J A and Svendsen N B 1992 Calculation of pressure fields from arbitrarily shaped, apodized, and excited ultrasound transducers *IEEE Trans. Ultrason. Ferroelectr. Freq. Control* **39** 262–7
[12] Goodman J W 1976 Some fundamental properties of speckle *JOSA.* **66** 1145–50
[13] Thijssen J M 2003 Ultrasonic speckle formation, analysis and processing applied to tissue characterization *Pattern Recognit. Lett.* **24** 659–75
[14] Mattausch O and Goksel O 2017 Image-based reconstruction of tissue scatterers using beam steering for ultrasound simulation *IEEE Trans. Med. Imaging* **37** 767–80
[15] Boyd S, Parikh N, Chu E, Peleato B and Eckstein J 2011 Distributed optimization and statistical learning via the alternating direction method of multipliers *Foundations and Trends® in Machine learning* **3** 1–122
[16] Yang J and Zhang Y 2011 Alternating direction algorithms for \ell_1-problems in compressive sensing *SIAM J. Sci. Comput.* **33** 250–78
[17] Rudin L I, Osher S and Fatemi E 1992 Nonlinear total variation based noise removal algorithms *Physica D* **60** 259–68
[18] Mohana Shankar P 2000 A general statistical model for ultrasonic backscattering from tissues *IEEE Trans. Ultrason. Ferroelectr. Freq. Control* **47** 727–36
[19] Kleiner D E *et al* 2005 Nonalcoholic Steatohepatitis Clinical Research N. Design and validation of a histological scoring system for nonalcoholic fatty liver disease *Hepatology* **41** 1313–21
[20] Yu H 2020 Scanning acoustic microscopy for material evaluation *Appl Microsc.* **50** 25
[21] Dencks S and Schmitz G 2023 Ultrasound localization microscopy *Z. Med. Phys.* **33** 292–308
[22] Miura K and Fukushi Y 2021 Scanning acoustic microscopy imaging of cellular structural and mechanical alterations from external stimuli *Heliyon.* **7** e07847
[23] Lin C Y, Cao L H, Wang J W, Zheng W, Chen Y, Feng Z Z, Li A H and Zhou J H 2013 Ultrasonic spectrum analysis for *in vivo* characterization of tumor microstructural changes in the evaluation of tumor response to chemotherapy using diagnostic ultrasound *BMC Cancer* **13** 302
[24] Zhou Z, Wu W, Wu S, Jia K and Tsui P H 2017 A review of ultrasound tissue characterization with mean scatterer spacing *Ultrason. Imaging* **39** 263–82
[25] Pensa J *et al* 2024 Evaluation of prostate cancer detection using micro-ultrasound versus MRI through co-registration to whole-mount pathology *Sci. Rep.* **14** 18910
[26] Kinnaird A *et al* 2025 Microultrasonography-guided vs MRI-guided biopsy for prostate cancer diagnosis: the OPTIMUM randomized clinical trial *JAMA* **333** 1679–87
[27] Wu W *et al* 2024 Experimental validation and clinical feasibility of 3D reconstruction of coronary artery bifurcation stents using intravascular ultrasound *PLoS One* **19** e0300098
[28] Wollborn J, Schuler A, Sheu R D, Shook D C and Nyman C B 2023 Real-time multiplanar reconstruction imaging using 3-dimensional transesophageal echocardiography in structural heart interventions *J. Cardiothorac. Vasc. Anesth.* **37** 570–81
[29] Cole A D, Roshankhah R, Blackwell J, Montgomery S A, Egan T M and Muller M 2023 Random matrix theory to quantify micro-structural changes in rodent lungs due to pulmonary diseases *J. Acoust. Soc. Am.* **153** A188–188
[30] Dalecki D, Mercado K P and Hocking D C 2016 Quantitative ultrasound for nondestructive characterization of engineered tissues and biomaterials *Ann. Biomed. Eng.* **44** 636–48
[31] Mamou J and Oelze M L (ed) 2023 *Quantitative Ultrasound in Soft Tissues* 2 ed (Springer) 307
[32] Parikh N and Boyd S 2014 Proximal algorithms *Foundations and trends® in Optimization* **1** 127–239